IMAGING

Bone CLARITY: Clearing, imaging, and computational analysis of osteoprogenitors within intact bone marrow

Alon Greenbaum,[1]* Ken Y. Chan,[1]* Tatyana Dobreva,[1] David Brown,[1] Deepak H. Balani,[2] Rogely Boyce,[3] Henry M. Kronenberg,[2] Helen J. McBride,[3] Viviana Gradinaru[1]†

Bone tissue harbors unique and essential physiological processes, such as hematopoiesis, bone growth, and bone remodeling. To enable visualization of these processes at the cellular level in an intact environment, we developed "Bone CLARITY," a bone tissue clearing method. We used Bone CLARITY and a custom-built light-sheet fluorescence microscope to detect the endogenous fluorescence of Sox9-tdTomato$^+$ osteoprogenitor cells in the tibia, femur, and vertebral column of adult transgenic mice. To obtain a complete distribution map of these osteoprogenitor cells, we developed a computational pipeline that semiautomatically detects individual Sox9-tdTomato$^+$ cells in their native three-dimensional environment. Our computational method counted all labeled osteoprogenitor cells without relying on sampling techniques and displayed increased precision when compared with traditional stereology techniques for estimating the total number of these rare cells. We demonstrate the value of the clearing-imaging pipeline by quantifying changes in the population of Sox9-tdTomato–labeled osteoprogenitor cells after sclerostin antibody treatment. Bone tissue clearing is able to provide fast and comprehensive visualization of biological processes in intact bone tissue.

INTRODUCTION

The mammalian skeletal system consists of numerous bones of varying shapes and sizes that provide support to the body and protect internal organs from external physical stress (*1*, *2*). Different bone types harbor specialized physiological processes that are key for proper development and survival of the organism, such as replenishment of hematopoietic cells, growth, and remodeling of the bone during healthy and diseased states (*3*–*6*). Traditionally, these processes have been investigated through methods that provide zero-dimensional (0D) or 2D information, such as fluorescence-activated cell sorting or analysis of histological sections. Quantitative 3D data of geometric features, such as volume and number of cells, can be obtained from histological sections with unbiased stereological methods. Although statistically robust, these methods are labor-intensive and provide no visualization of the 3D structures. The need for methods that provide 3D information to study the bone has long been recognized. Although methods, such as serial sectioning and milling, are valuable tools for understanding the structure of bone at the tissue level, these are destructive techniques that do not provide information at the cellular level and cannot be easily combined with other methods, such as immunohistochemistry, to characterize cellular processes (*7*, *8*).

CLARITY (Clear Lipid-exchanged Acrylamide-hybridized Rigid Imaging/Immunostaining/In situ hybridization–compatible Tissue hYdrogel) was originally developed for soft tissues, such as the brain (*9*); recently, there has been a surge in optical clearing methods for a variety of applications (for example, profiling of tumor biopsies and brain tissue) (*9*–*15*). Bone is a more complex histological sample, owing to its hard (mineral) and soft (bone marrow) tissue, and accordingly, osseous tissue has remained a challenge, despite some promising developments reviewed in (*14*, *16*). One method for investigating intact bones and their 3D microenvironments at submicrometer resolution is to render the tissue optically transparent. Bone transparency can be accomplished by coupling refractive index (RI) matching reagents with removal of minerals and lipids that scatter light. Most bone clearing literature is based on solvent clearing methods (*17*–*20*). These methods focus on RI matching and solvation of some lipids but do not remove minerals (*14*, *16*). In general, these solvent-based clearing methods have achieved an imaging depth of about 200 μm using two-photon microscopy (*18*). Murray's clearing method was recently modified to clear bisected long bones and achieved an imaging depth of about 600 μm with confocal microscopy (*21*). Despite these advances, manipulation and subsampling of the bone is required for deep imaging, thus disrupting the intact bone architecture. A key limitation of Murray's clearing method and its variants is that they quench endogenous fluorescence, minimizing their application with transgenic fluorescent reporter lines, which are used to highlight key cell populations within the bone and marrow. Consequently, there is a need for a clearing method that maintains the intact bone structure, preserves endogenous fluorescence, and allows deeper imaging within intact bone.

In our previous work (*15*), we noticed that decalcification (deCAL) of bones by EDTA could, in principle, expand CLARITY applications to osseous tissues, but we only achieved modest optical access (200 to 300 μm). Here, we introduce Bone CLARITY, a specialized protocol that incorporates continuous convective flow during the clearing process, amino alcohol to minimize tissue autofluorescence (*22*, *23*), and an imaging procedure that minimizes RI variations in light-sheet microscopy. These improvements allowed us to achieve whole-bone clearing with an imaging depth of up to about 1.5 mm while maintaining native tdTomato fluorescence and a signal-to-noise ratio (SNR) that permitted detection and 3D placement of single cells. We present a comprehensive platform based on whole-bone clearing, light-sheet imaging with a custom-built microscope, and dedicated computational methods for counting fluorescently labeled cells. We use this trio of methods to visualize and quantify the total number of osteoprogenitors contained within a volume of mouse bone and map their 3D spatial distribution in response to a sclerostin antibody (Scl-Ab), a bone-forming agent.

[1]Division of Biology and Biological Engineering, California Institute of Technology, Pasadena, CA 91125, USA. [2]Endocrine Unit, Massachusetts General Hospital, Harvard Medical School, Boston, MA 02114, USA. [3]Comparative Biology and Safety Sciences, Amgen, Thousand Oaks, CA 91320, USA.
*These authors contributed equally to this work.
†Corresponding author. Email: viviana@caltech.edu

RESULTS

Bone CLARITY renders intact bones transparent while preserving endogenous fluorescence

We developed and applied a bone clearing method to render the tibia, femur, and vertebral column of mice transparent for light microscopy investigation (Fig. 1A). The key steps of the sample preparation, including tissue clearing and autofluorescence removal, are outlined in Fig. 1B and fig. S1. The bone is decalcified to increase light and molecular penetration through the tissue while leaving a framework of bone matrix with similar structural characteristics to dense fibrous connective tissue. Bone CLARITY uses an acrylamide hydrogel to support the tissue structure and minimize protein loss before the delipidation step. The detergent SDS is used to remove lipids to minimize their light-scattering effects. We observed high autofluorescence in the bone marrow, one of the primary sites of heme synthesis. Because heme is strongly autofluorescent, in the final step of the process, we used the amino alcohol *N*,*N*,*N*′,*N*′-tetrakis(2-hydroxypropyl) ethylenediamine (*22*, *23*) to remove heme, which minimized marrow autofluorescence by about threefold (fig. S2). All of the above clearing stages were conducted on a temperature-controlled stir plate that provided continuous convective flow (fig. S3; auxiliary design file). This accelerates and improves the clearing process for entire organs compared with passive clearing (*15*). Notably, the samples did not change size during the clearing process (fig. S4).

The imaging of intact bone tissue using a point-scanning method (such as a confocal microscope) poses an operational challenge because acquisition times are prolonged, with concomitant photobleaching (*24*–*26*). To address this, we built a custom light-sheet fluorescence microscope (LSFM) with confocal slit detection (fig. S5) (*15*, *27*). To modify the LSFM to image bones, we added an additional light-sheet path to illuminate the bones from two opposite directions. This additional light path improved optical access to areas containing a high percentage of cancellous bone, which typically scatter light more extensively and consequently lower the SNR. Given a particular depth scan, the sample is illuminated by only one of the two light-sheet paths, whichever provides the better contrast. We use only one illumination path per depth scan because there is always one illumination direction that scatters less light and thus provides superior image quality. To minimize RI mismatch between the objective lens and the bones, we directly immersed the samples in the immersion chamber without the use of a quartz cuvette to hold the sample. If RI variations still persist, the position of the detection objective is changed for each tile and specific depth along the *Z*-scan, to mitigate any resulting out-of-focus aberrations. The LSFM captures images at a frame rate of 22 frames per second (16-bit depth) and produces 0.176 gigabytes (GB) of imaging data per second. Large data sets are thus acquired for each imaged bone (50 to 500 GB). To manage these large data sets, we designed a computational pipeline that includes image stitching, automatic detection of individual cells, and volume-of-interest (VOI) rendering for analysis (Fig. 1C).

To validate the protocol, we applied our clearing and imaging method to locate progenitor cells in the long bones and vertebrae of transgenic reporter mice. A Sox9CreER transgenic mouse line was used in which, upon tamoxifen injection, multipotent osteoblast and chondrocyte progenitor cells express tdTomato (*1*, *28*). We visualized the endogenous fluorescence of Sox9$^+$ cells using Bone CLARITY (Fig. 1, D and E). Quantification of the imaging depth in different regions of the tibia, femur, and vertebral body showed that we were able to image through the diaphysis of the femur (movie S1) and tibia (movie S2) and the entire vertebral body (movie S3). Furthermore, we were able to reliably detect Sox9$^+$ cells up to about 1.5 mm deep into the bones (fig. S6). Collectively, Bone CLARITY coupled with LSFM and the data processing pipeline is an effective clearing, imaging, and data processing protocol for investigating intact mouse bones.

Semiautomated computational pipeline quantifies Sox9$^+$ cells in mouse tibia and femur

To demonstrate that biological environments can be observed and quantified with Bone CLARITY, we first counted Sox9$^+$ cells in the tibia and femur. We found that Bone CLARITY allows for detection and quantification of individual Sox9$^+$ cells in 3D (Fig. 2A), some of which appear associated with small blood vessels. Owing to the large VOI (Fig. 2A; gray surface), we created a semiautomated cell detection algorithm (Fig. 2B and fig. S7). The algorithm divides the 2D images that make up the *Z*-stack (or depth scan) into *n* small overlapping regions, and then adaptively thresholds the 2D images into binary images on the basis of the local mean and SD of fluorescence. The resulting binary 2D images are further subjected to morphological operations to eliminate noise and discontinuity within a cell. All of the 2D binary images are then combined into a 3D matrix. From the 3D matrix, only volumes that fit the properties of a Sox9$^+$ cell are maintained, thus avoiding erroneous counting of large blood vessels or small autofluorescence artifacts. All cells outside the user-defined VOI (Fig. 2A) are discarded. The cell candidate centroid locations are then imported to 3D visualization software for manual quality control. During the quality control stage, the annotator reviews the entire 3D volume and corrects the automatic results by marking false-negative cells and omitting false-positive cells. Therefore, at the end of the quality control stage, the cell counts are equivalent to cell counts that were performed manually. According to our experiments, a fully automatic pipeline only achieves 52% sensitivity and 36% precision on average. Note that removing false positives is a faster operation in the 3D visualization software than adding false negatives; therefore, the value of sensitivity outweighs the need for precision.

We quantified the number of fluorescently labeled Sox9$^+$ cells in the femur and tibia of Sox9CreER mice versus two control groups: Sox9CreER mice without tamoxifen administration and wild-type mice without the transgenes (Fig. 2C). The analyzed volume for each group was comparable (fig. S8). The cell counts in the Sox9CreER group without tamoxifen administration can be attributed to leakage of the reporter line because there was no visible expression of tdTomato in the wild-type control samples (*29*). Qualitatively, this expression leakage can be observed in fig. S9, where the expression of the tdTomato signal is compared between the experimental group and the two control groups. We next quantified the cell distribution as a function of distance from the periosteal surface along the longitudinal plane (schematic in Fig. 2D). On the basis of our analysis, most of the cells in the diaphysis reside adjacent to the endocortical surface, with mean distances from the periosteal surface of about 136.9 and 143.6 μm for the tibia and femur, respectively (Fig. 2E). This result supports similar findings in (*30*) and validates Bone CLARITY as a reliable method to resolve and quantify individual cells in intact bone and marrow spaces. Note that Bone CLARITY is not limited to visualizing cell populations in transgenic animals only and that antibody staining is also feasible (fig. S10). However, for maximum penetration of the antibody into the bone for secondary staining, it is recommended to bisect the bone before the clearing process.

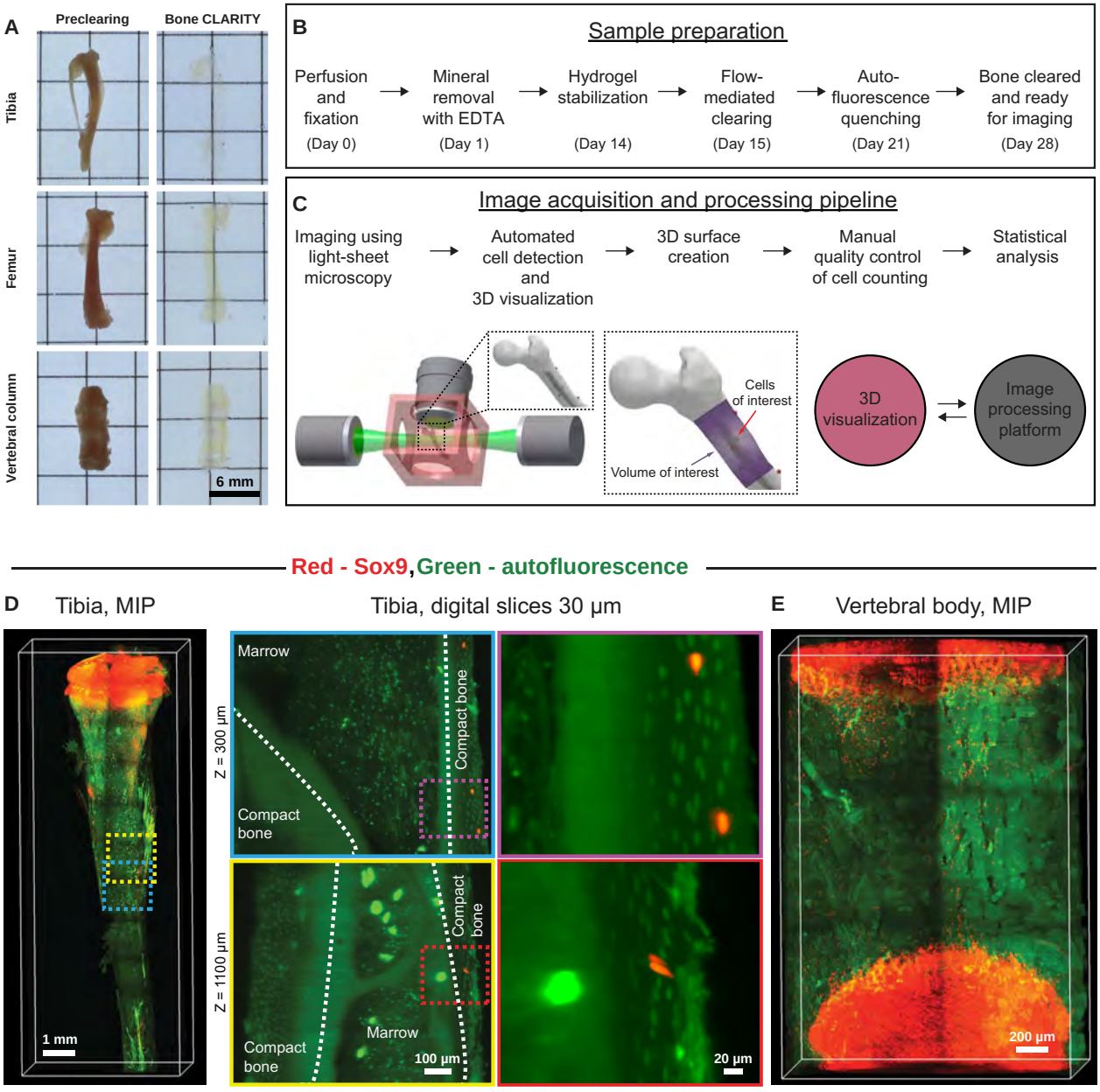

Fig. 1. Bone CLARITY renders intact bones transparent while preserving endogenous fluorescence. (**A**) Micrographs of mouse tibia, femur, and vertebral column before and after CLARITY. Bones were rendered transparent using Bone CLARITY. (**B**) Block diagram outlining of the key steps of Bone CLARITY sample preparation. The procedure includes the following: demineralization, hydrogel stabilization, lipid removal via constant flow, and autofluorescence removal. (**C**) A schematic diagram of the imaging and computational pipeline that uses the interface between 3D visualization and image-processing programs. (**D**) Maximum intensity projection (MIP) fluorescence image of the tibia and zoomed-in digital slices (red, Sox9; and green, autofluorescence). Using Bone CLARITY, bones were imaged from one end to the other in the diaphysis (magnified images) and about 1.5 mm deep into the epiphysis (movies S1 to S3). Dotted yellow and blue boxed regions in the MIP represent the area of zoom in the digital slices (30 µm thick). The purple and red dotted boxed regions in the digital sections represent the area that is shown with further higher magnification. The white dotted lines represent the boundaries of the compact bone. (**E**) MIP fluorescence image of the vertebral body.

Bone clearing can complement section-based stereology

Design-based stereology is the gold standard method to quantify total cell numbers and densities in organs while preserving spatial information (*31*, *32*). Stereology relies on statistical sampling methods. Systematic uniform random sampling (SURS) is a frequently used sampling method that efficiently reduces the variance of the estimate compared with random sampling. SURS obtains histological sections from an organ to reduce the amount of tissue for analysis. SURS samples at regular uniform intervals with the first sample collected at a random position within the first interval (*33*, *34*). The number of cells in a tissue volume is a 0D geometric feature. Thus, to avoid bias due to cell size or shape, a probe based on two thin physical sections or optical planes separated by a known distance (disector) is used to accomplish quantification (*35*, *36*). Cells are typically counted in a known fraction of the organ, which allows for an estimation of the total number of cells in the entire organ (*37*). The spatial

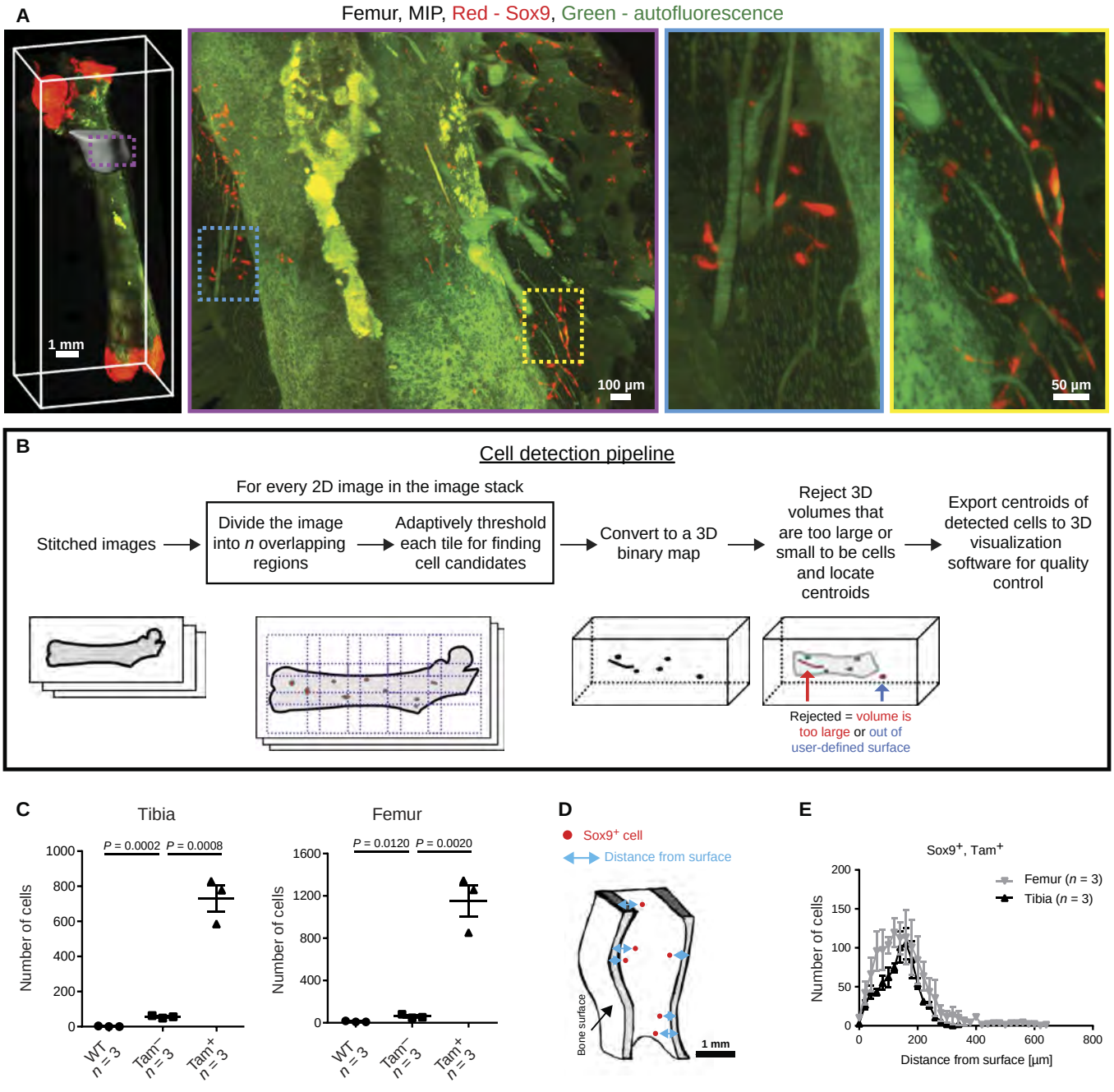

Fig. 2. Bone CLARITY enables quantification of fluorescently labeled Sox9$^+$ cells in the mouse tibia and femur. (**A**) Femur MIP fluorescence image and magnified images showing single Sox9$^+$ cells in the vicinity of the third trochanter (red, Sox9; and green, autofluorescence).The gray surface surrounding the femur represents an overlay of the VOI; only the cells that reside within the VOI are quantified. The purple, blue, and yellow boxed regions in the MIP represent progressive magnification. (**B**) Block diagram of the semiautomated cell detection pipeline where cell candidates are identified via adaptive thresholding and their volume calculated. A predetermined selection criterion based on cell volume is used to reject blood vessels or any detected blobs that are too large or too small. (**C**) A comparison of fluorescently labeled Sox9$^+$ cell numbers between the experimental group [tamoxifen-positive (Tam$^+$)] and control groups [wild-type (WT) and tamoxifen-negative (Tam$^-$)] for the femur and tibia. $n = 3$ animals per group; 1 bone per animal. For tibia: WT versus Sox9$^+$;Tam$^-$, $P = 0.0002$ and Sox9$^+$;Tam$^-$ versus Sox9$^+$;Tam$^+$, $P = 0.0008$. For femur: WT versus Sox9$^+$;Tam$^-$, $P = 0.012$ and Sox9$^+$;Tam$^-$ versus Sox9$^+$;Tam$^+$, $P = 0.002$. All values are means ± SEM; two-tailed, unpaired t test. (**D**) Schematic showing how the distance of Sox9$^+$ cells from the surface is calculated. (**E**) The distribution of the number of Sox9$^+$ cells versus the distance from the bone surface. All values are means ± SEM.

distribution of cells can also be obtained using second-order stereological methods (*38*).

Applying stereological methods to cleared organs offers notable time-saving because clearing precludes the need for labor-intensive sectioning. Using the Bone CLARITY method and our 3D counting scheme, we investigated the variability in stereology estimates as a function of the number of slices for both SURS and simple random sampling in stereology experiment simulations. Figure 3A shows

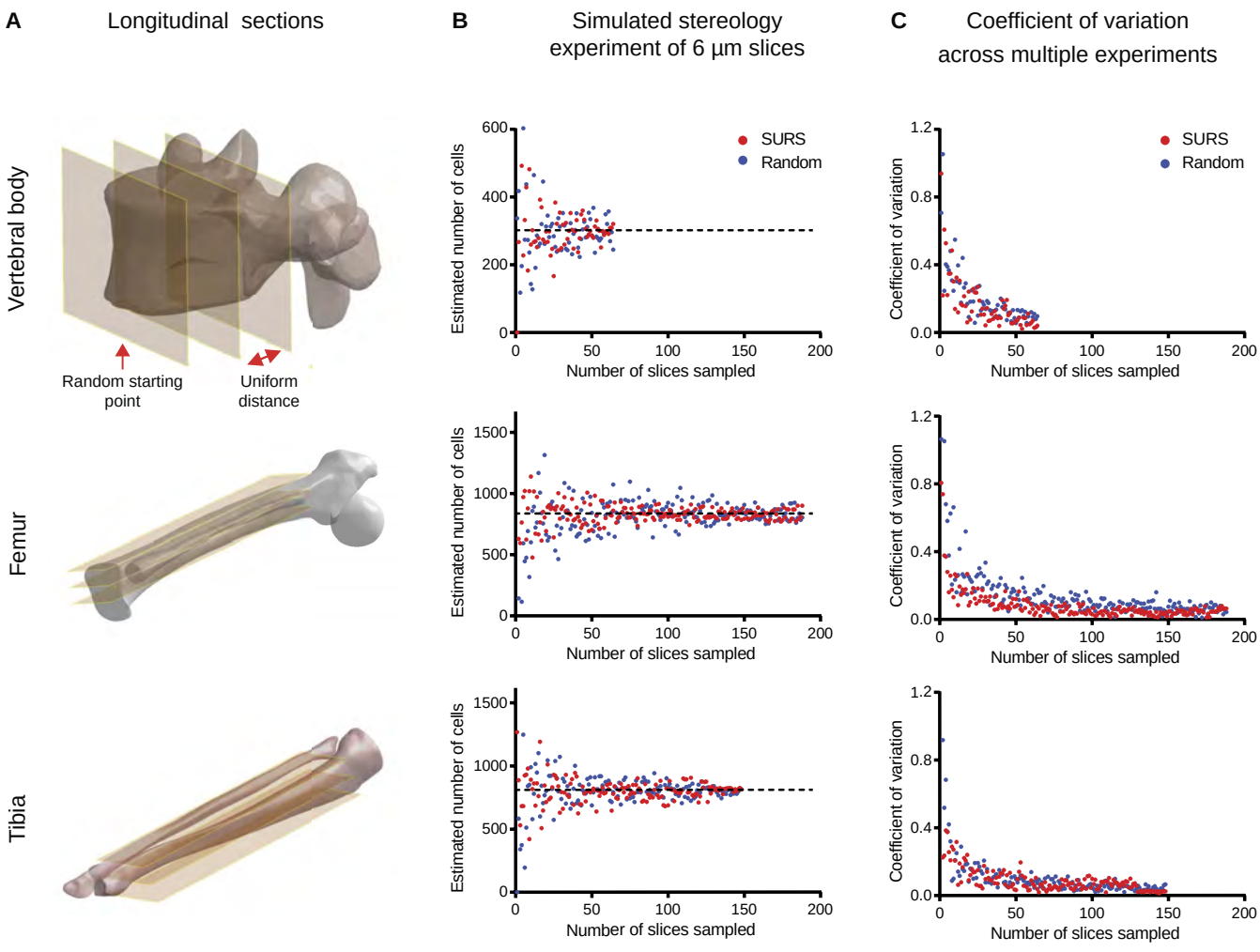

Fig. 3. Using intact tissue clearing methods reduces cell estimate variability compared with traditional tissue sectioning methods. (**A**) Schematic diagram showing the sample selection procedure for systematic uniform random sampling (SURS) of the mouse femur, tibia, and vertebral body. *n* uniformly spaced 2D sections are selected, offset by a random starting distance. The red single arrow indicates the random starting point, whereas the double arrow indicates the distance between the 2D sections. (**B**) Sox9$^+$ cell number estimation as a function of the number of sampled sections in a representative simulated stereology experiment using both SURS (red dots) and simple random sampling (blue dots). To simulate a stereology experiment, we used the cell density in the sampled sections to interpolate the cell number in the entire VOI. The black dashed line represents the ground truth, cell number based on the entire volume. (**C**) The coefficient of variation of five simulated stereology cell number estimates as a function of the number of sampled slices using SURS (red dots) and simple random sampling (blue dots).

one representative selection of *n* random uniformly spaced sections for a simulated SURS experiment in the femur, tibia, and vertebral body. Figure 3B shows the estimates for the cell count of an entire VOI based on *n* sampled slices, and Fig. 3C shows the coefficient of variation of simulated stereology experiments that were conducted with *n* slices. To estimate the coefficient of variation for each *n* representative slices, we conducted five simulated stereology experiments. As expected in these simulations, variance decreased rapidly with increasing number of slices for femur, tibia, and vertebra. Precision of the stereological estimate would likely be improved with proportionator sampling, a form of nonuniform sampling better suited to rare structures (*39*). Nonetheless, the 3D counting method offers several advantages for quantifying rare cellular populations: the ability to detect subtle changes that might be overlooked because of sampling variance, elimination of the need for sectioning, and 3D visualization.

Scl-Ab increases the number of Sox9$^+$ cells in the vertebral column

We next applied Bone CLARITY to the vertebral column, a bone that is highly susceptible to fractures due to osteoporosis (*40*) and whose complex geometry is particularly difficult to probe with traditional sectioning-based methods. We cleared and imaged the vertebrae from mice and focused on the fourth lumbar vertebral body (L4), which is dense, opaque, and predominately composed of cancellous bone. Figure 4 (A and B) shows schematics of lateral and transverse cuts from a representative vertebra. Figure 4B also shows the approximate locations (dashed lines) of the digital sections (30 µm thick) that are shown in Fig. 4C. The lateral processes that extrude from the vertebral body can be seen in the horizontal edges of the 650-µm section. These processes were excluded from the cell counts, as illustrated by the representative VOI (Fig. 4D). In addition, careful attention was given to ensure the exclusion of the intervertebral discs

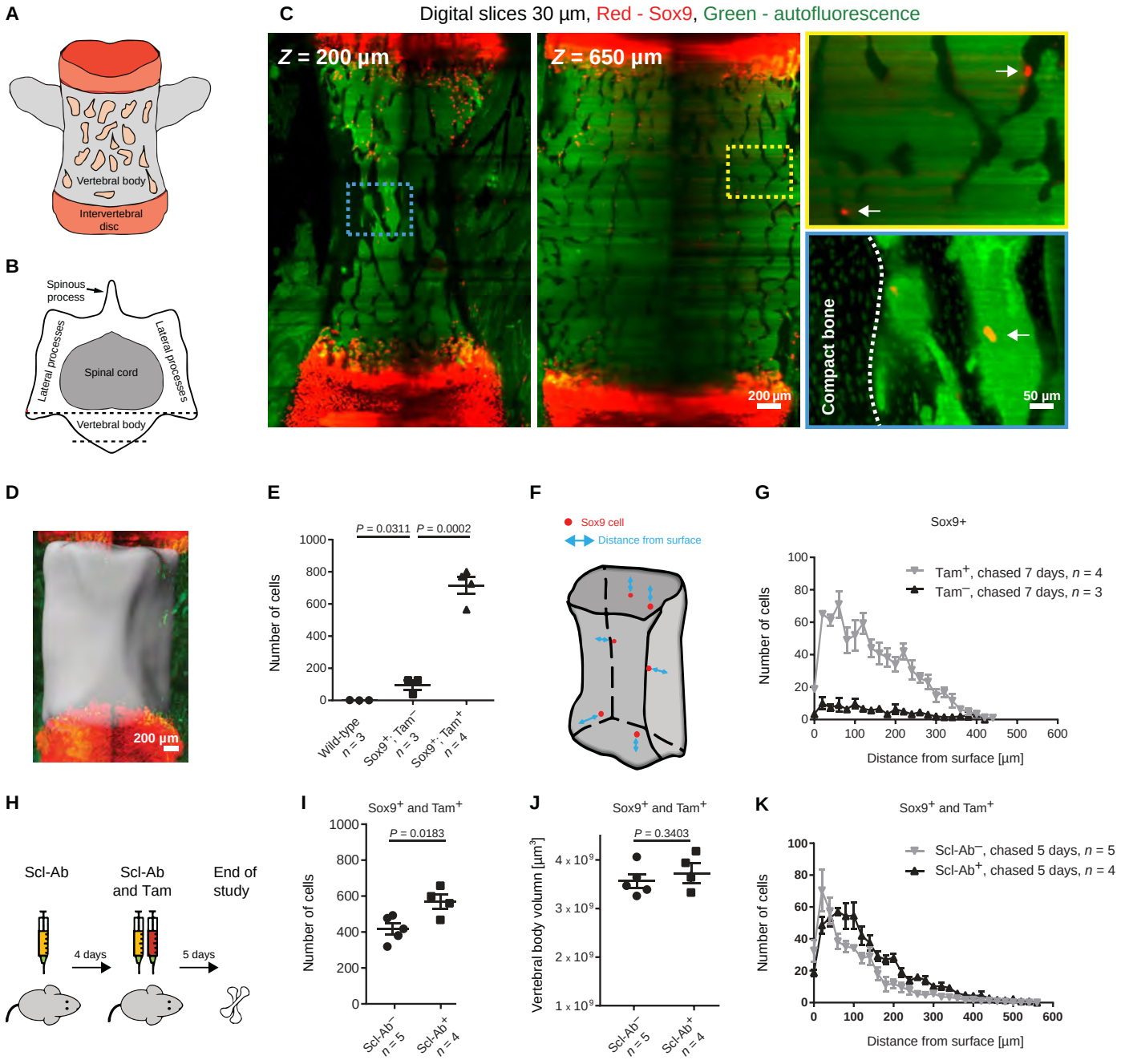

Fig. 4. Bone CLARITY enables quantification of the effect of Scl-Ab on the number of fluorescently labeled Sox9 cells in the mouse vertebra. (**A**) Schematic depicting the lateral view of a mouse vertebra. The intervertebral disc is labeled in red; chondrocytes proliferate there after differentiation from tdTomato-Sox9$^+$ cells (chased for 7 days). The marrow is represented in light orange. (**B**) Transverse view of an L4 vertebra. The cell counts are isolated to the vertebral body, and the dashed lines approximate the locations of the sections shown in (C). (**C**) Digital sections (30 µm thick) at different depths along the vertebral body (Z = 200 and 650 µm) (red, Sox9; and green, autofluorescence). The intervertebral discs are notable at the vertical boundaries of the images. The white arrows in the color-coded magnified images point to Sox9$^+$ cells, and the dashed white line in the magnified image marks the interface between the compact bone and the marrow. (**D**) Micrograph of the mouse vertebral body showing a representative VOI (gray surface), which does not include the intervertebral discs. (**E**) Total cell number in tamoxifen-injected mice versus control groups. For WT versus Sox9$^+$;Tam$^-$, P = 0.0311 and Sox9$^+$;Tam$^-$ versus Sox9$^+$;Tam$^+$, P = 0.0002. (**F**) Schematic showing how cell distance from surface is determined on a transparent vertebral body VOI. For each cell, the distance is defined as the shortest path to the surface in any direction. (**G**) The distribution of Sox9$^+$ cells as a function of distance from the endocortical surface. (**H**) Schematic of the Scl-Ab experimental timeline. (**I**) Quantification of the number of cells within the VOI in the Scl-Ab and vehicle-treated mice. For Sox9$^+$;Tam$^+$;Scl-Ab$^-$ versus Sox9$^+$;Tam$^+$;Scl-Ab$^+$, P = 0.0183. (**J**) No significant change in the vertebral body volume was observed between the Scl-Ab group and the vehicle group. For Sox9$^+$;Tam$^+$;Scl-Ab$^-$ versus Sox9$^+$;Tam$^+$;Scl-Ab$^+$, P = 0.3403. (**K**) The distribution of Sox9$^+$ cells as a function of distance from the endocortical surface. All values are means ± SEM; two-tailed, unpaired t test.

and cartilage endplates from the VOI because they are both primarily populated by chondrocytes. These chondrocytes express Sox9 and are tdTomato$^+$ after tamoxifen administration and thus require careful exclusion for accurate cell counts of fluorescently marked osteoprogenitors. The quantification of vertebral Sox9-tdTomato cells after tamoxifen administration versus the two control groups, Sox9CreER mice without tamoxifen administration and wild-type mice, can be seen in Fig. 4E. Again, we observed that the Sox9CreER transgenic animals without tamoxifen administration display mild leakage of tdTomato expression (Fig. 4E and fig. S9). Overall, similar to the cell distribution results presented for the tibia and femur, the Sox9$^+$ cells were primarily located adjacent to the endocortical surface (Fig. 4, F and G), with a mean distance of 138.8 and 137.6 μm for the Tam$^-$ and Tam$^+$ groups, respectively.

We next tested the effects of Scl-Ab on the total number of Sox9$^+$ cells in the vertebral column. Sclerostin is an extracellular inhibitor of the canonical Wnt signaling pathway and is highly expressed in osteocytes. Inhibition of sclerostin leads to activation of canonical Wnt signaling in the osteoblast lineage, resulting in a rapid but transient marked increase in osteoblast number and corresponding bone formation (*41*). Although the early marked increase in osteoblast number is considered to be at least in part due to activation of bone lining cells (*42*), the contribution of osteoprogenitors to this early increase in osteoblast number is unclear. Although a decrease in osteoprogenitors has been demonstrated to be associated with the attenuation of bone formation that occurs with long-term Scl-Ab treatment in rats, stereological methods have not detected effects on progenitor number coincident with the maximal increase in osteoblast number. To gain insight into the acute effects of Scl-Ab on osteoprogenitors, we conducted an experiment as outlined in Fig. 4H. On day 1, Sox9CreER mice were injected with Scl-Ab (100 mg/kg subcutaneously). Four days after, we provided a second dose of Scl-Ab along with tamoxifen to label Sox9$^+$ cells with tdTomato. We euthanized the animals 5 days later and cleared the bones using Bone CLARITY. After performing blinded quantification of Sox9$^+$ cells, we observed an increase in the total number of Sox9$^+$ cells in the vertebral body 9 days after initial Scl-Ab treatment versus the vehicle control group (Fig. 4I). We did not observe any significant changes to the vertebral body volume (Fig. 4J) between the experimental and control groups at this early time point. These results demonstrate that there is an increase in osteoprogenitors that are likely recruited to the bone surface to contribute to the increase in osteoblast number. The distribution of cells as a function of distance from the surface can be seen in Fig. 4K, with mean distances of about 99.9 and 137.8 μm for the vehicle and treated groups, respectively.

DISCUSSION

In the bone remodeling process, bone health is maintained through continuous cycles of bone resorption by osteoclasts and bone formation by osteoblasts. Imbalances in these physiological processes can lead to various bone diseases, such as osteoporosis, which affect millions of people in the United States alone (*40*, *43*). To gain better insight into potentially effective treatments for osteoporosis, it is imperative to study the physiological processes that occur in healthy and diseased bone and understand its molecular and cellular mechanisms within the 3D microenvironment. We demonstrate that the Bone CLARITY technique renders the tibias, femurs, and vertebral bodies of mice optically transparent while preserving bone morphology and an endogenous fluorescent reporter signal. In addition to matching the RI of the tissue, Bone CLARITY also removes minerals and lipids, thus enabling us to reconstruct a whole vertebral body and the entire diaphysis from the tibia and femur.

For maximum impact, clearing and imaging platforms need to be easy to use and scalable. The trio of methods presented here has a few limitations in its current rendering that could be improved in the future, such as the addition of antibody staining to the clearing workflow, reducing processing time, and overcoming the technical barriers of acquiring and analyzing big data sets. Antibody staining of an intact bone is challenging because of poor penetration by relatively large antibodies. To improve antibody penetration, we bisected and cleared half of a tibia and femur. In the bisected and cleared bones, the antibody penetrated up to 400 μm from the bone surface and showed high specificity and SNR (fig. S10). The use of small-molecule staining methods [for example, single-molecule hybridization chain reaction (*44*)] could allow the labeling of intact bones while achieving improved staining depths. Meanwhile, the ability to retain and detect endogenous fluorescence has proven highly enabling, although the gentle clearing reagents used in Bone CLARITY do introduce a compromise in processing time (28 days). Using faster decalcification agents, such as formic acid, might shorten the current deCAL time of 14 days, although the fluorescent proteins generated by the reporter genes used in this study might lose their fluorescence under acidic conditions (*24*, *45*). Delipidation is also a lengthy stage in Bone CLARITY but necessary to reduce scattering from lipids not only present in the mineralized bone tissue but also highly abundant within the bone marrow. Consequently, delipidation ensures high-quality optical access deep in the bone. Although the use of customized microscopy and software might not be easy to implement in a nontechnical setting, commercial LSFM systems with a streamlined user interface and associated software are rapidly evolving to support the types of applications described here. For data processing, we found that fully automated cell detection algorithms were difficult to apply within cleared tissue. SNR variations arising from nonuniform illumination and fluorescence detection within the bone resulted in unsatisfactory precision, necessitating manual quality control. The simple automated tools that we developed are fast and adaptive and, in general, are able to save annotator time while improving precision and reducing error; however, more work is required to achieve a reliable, fully automated algorithm for cell counting. In general, data handling, visualization, and analysis would benefit from individual developers sharing their code in an open-source environment, which would allow the scientific and medical community to efficiently customize software relevant for the application at hand.

Bone CLARITY enables clearing of mouse bones while retaining the integrity of the bone marrow and endogenous fluorescence. After clearing, we achieved 3D reconstructions of a vertebral body and long bone diaphyses and attained an imaging depth of about 1.5 mm for the epiphysis of long bones. Using a computational pipeline to process large data sets and detect single cells in bone, we mapped the spatial distribution of osteoprogenitor cells. In addition, we demonstrated the advantages of 3D methods in estimating rare cell populations that are not readily amenable to sampling by traditional stereology methods. Note that combining traditional stereology methods with tissue clearing techniques can be advantageous, especially in cases where quantification of complicated structural elements cannot be done automatically. Therefore, subsampling is advantageous for manual quantification within a reasonable time frame. Last, to further demonstrate the use of our clearing method, we treated a cohort of adult reporter mice with Scl-Ab, a bone-forming agent, for 9 days. Previous

stereological studies in rats treated with Scl-Ab for 8 days revealed a marked increase in total osteoblast number in the vertebrae coincident with increased bone formation but no significant effect on bone progenitor numbers (*41*). After 9 days of treatment in mice, we found that the total number of osteoblast progenitor cells increased by 36% compared with the control group. This result was not surprising based on the literature (*41*), but it has been challenging to demonstrate using stereological methods given the rarity of osteoprogenitor cells, particularly in the vertebrae. This underscores the greater sensitivity of our clearing, imaging, and data-processing protocol for quantifying rare cell populations and using lineage tracing to mark progenitors, as opposed to immunophenotyping in tissue sections. Overall, continued developments in tissue clearing (*14*, *16*, *46*), imaging, and data analysis can facilitate translational research that will provide insight into the efficacy and safety of new bone-modulating drugs by profiling their effects on progenitor cell populations.

Other fields might also benefit from applying the bone clearing technique, such as neuroscience. Removal of the skull damages the interface between the skull and the underlying vascular bed and neuronal tissue. Preservation of this interface would be beneficial for studying the lymphatic vessels residing within it, assessing head trauma (for example, percussive injuries), and characterizing the positioning of head-mounted brain implants in an intact environment (*47*, *48*).

MATERIALS AND METHODS

Study design

The objective of this study was to enable the visualization and quantification of cell population in an intact bone tissue by developing and integrating tissue clearing, fluorescence microscopy, and a computation pipeline. Experimental and control animal cohorts were chosen based on preliminary data that suggested a large effect size. All transgenic animals used in this study are as described in the Animals section. All wild-type animals used in this study were C57BL/6. To characterize the density of $Sox9^+$ cells and distribution within the femur, tibia, and vertebral column, male transgenic animals of 6 to 7 weeks of age received a 2 mg of tamoxifen intraperitoneally on day 1 of the experiment to enable expression of a native fluorescent gene for 7 days before culling. For the study of the effects of Scl-Ab on total number of osteoprogenitor cells, a cohort of 7-week-old male transgenic animals were treated with Scl-Ab at 100 mg/kg (subcutaneously) on day 1 and again at 100 mg/kg (subcutaneously) 4 days later with tamoxifen induction at 2 mg (intraperitoneally), before culling on day 9 of the study. The Scl-Ab was provided by Amgen. During cell counting, all manual quantification is performed in a blind manner to eliminate observer bias. Animals were randomly assigned to groups for experiments. Raw data values for cell counts are reported in the Supplementary Materials.

Animals

A transgenic Sox9-CreERT2 mouse (RIKEN BioResource Center, # RBRC05522) was crossed to a Rosa26-loxP-stop-loxP-tdTomato (R26R-tomato, JAX7914) reporter mouse to generate Sox9-CreERT2-R26-tdt. Sox9-CreERT2-R26-tdt mice aged 6- to 7-week-old were used in the experiments involved in labeling Sox9 cells (n = 18). The labeling was achieved by intraperitoneal injection of 2 mg of tamoxifen, which was dissolved first in 100% ethanol then in sunflower seed oil (Sigma-Aldrich, #S5007) overnight at 60°C. Mice were genotyped by polymerase chain reaction. All mice were analyzed in mixed backgrounds. Mice were group-housed in sterile, ventilated microisolator cages on corn cob bedding in a facility accredited by the Association for Assessment and Accreditation of Laboratory Animal Care. All procedures were conducted in compliance with the *Guide for the Care and Use of Laboratory Animals* approved by Massachusetts General Hospital's Institutional Animal Care and Use Committee. Animals were provided ad libitum access to pelleted feed (LabDiet 5010) and water (Standard drinking water of Boston, MA; pH 7.8) via Hydropac. Animals were maintained on a 12-hour light/12-hour dark cycle in rooms at 64° to 79°F with 30 to 70% humidity under pathogen-free conditions.

Bone deCAL CLARITY protocol

The clearing process is summarized in fig. S1. After euthanization, mice were perfused transcardially with 0.01 M phosphate-buffered saline (PBS) (Sigma-Aldrich, #P3813) followed by 4% paraformaldehyde (PFA) (VWR, #100496-496), and the femurs, tibias, and L3 to L5 vertebral columns were extracted. The bones were postfixed overnight in 4% PFA. To enhance clearing of hard-tissue, we extended the demineralization phase to 2 weeks with 10% EDTA (Lonza, # 51234) in 0.01 M PBS (pH 8). During the demineralization phase, samples were kept under constant stirring in histology cassettes (Electron Microscopy Sciences, #70077-W) at 4°C with fresh EDTA buffer exchanges daily. Next, the decalcified bones were embedded in a hydrogel matrix (A4P0), which consists of 4% acrylamide (Bio-Rad, #1610140), 0% PFA, and 0.25% thermoinitiator (Wako Chemicals, VA-044), in 0.01 M PBS overnight at 4°C. The samples were degassed through nitrogen gas exchange for 5 min and polymerized for 3 hours at 37°C. After structural reinforcement with the A4P0 hydrogel, delipidation was performed with 8% SDS in 0.01 M PBS (pH 7.4) for 4 or 5 days (vertebral body and long bones, respectively) at 37°C under constant stirring (fig. S3). The samples were then washed for 48 hours in 0.01 M PBS with three buffer replacements. The amino alcohol *N*,*N*,*N*′,*N*′-tetrakis(2-hydroxypropyl)ethylenediamine (Sigma-Aldrich, #122262-1L) was added at 25% w/v in 0.01 M PBS (pH 9) for 2 days at 37°C under constant stirring for the purpose of decolorization of the tissue through heme group removal. Last, the bones were washed with 0.01 M PBS for 24 hours and subsequently immersed in RI matching solution (RIMS). The bones were gradually immersed in RIMS (*15*) with an RI of 1.47 through daily stepwise RIMS exchange with RIMS 1.38, 1.43, and finally, 1.47.

Light-sheet microscopy imaging

Before imaging, the sample was placed in the LSFM sealed immersion chamber for at least 3 hours, allowing the RIMS solution in the chamber to equilibrate with the residue RIMS in the bone sample. To minimize optical aberrations, we measured the RI of the RIMS solution, and the correction collar on the objective lens (10× CLARITY objective lens with numerical aperture of 0.6; Olympus XLPLN10XSVMP) was set accordingly. To image the entire bone, we acquired multiple tiles with 10% overlap. Typically, the femur, tibia, and vertebral body required 13 × 5, 11 × 5, and 3 × 2 tiles, respectively (vertical × horizontal). In a calibration stage that took place before the scan, the following parameters were defined for each tile: (i) light-sheet illumination direction; the LSFM has two light sheets that illuminate the sample from opposite directions. Selecting the preferable illumination direction markedly reduced scattering. (ii) The start and end point of the *Z*-stack; this step was carried out to minimize the number of acquired images in an already big

data set (50 to 500 GB). (iii) The focus points of the detection objective along the scan were defined to mitigate RI variations along the scan that created out-of-focus aberrations. Once the calibration stage was completed, the bone was imaged with a frame rate of 22 frames per second and bit depth of 16 bits. The acquired data set size depends on the sampled voxel size. For a voxel size of $0.585 \times 0.585 \times 2\ \mu m^3$, the tibia and femur produced ~250 GB of data per color channel, whereas the vertebral body produced ~30 GB of data per color. Generally, the data sets are down-sampled after acquisition for processing; the typical voxel sizes are $1.17 \times 1.17 \times 2\ \mu m^3$ and $2.34 \times 2.34 \times 2\ \mu m^3$ for the vertebral column and long bones, respectively.

All experimental and control groups were imaged with the same laser power. For images that were acquired deep in the bone and when the SNR changed within the distance from the bone boundary, the contrast and gamma were adjusted in the displayed images. The gamma adjustment was performed to visualize cells that exhibit both low and high intensity within the same field of view. Images from the vertebra ($Sox9^+$ and Tam^+ group) are representative of 13 vertebrae from 13 mice. Images from the tibia and femur ($Sox9^+$ and Tam^+ group) are representative of five tibias and five femurs from five mice.

Statistical analysis

All statistical analyses were performed using GraphPad Prism version 7.01. For Figs. 2C and 4 (E, I, and J), mean values for each group were compared using an unpaired *t* test. In all graphs, data points per individual animal trial with the mean value and SEM are shown.

SUPPLEMENTARY MATERIALS

www.sciencetranslationalmedicine.org/cgi/content/full/9/387/eaah6518/DC1
Methods
Fig. S1. Bone CLARITY clearing process.
Fig. S2. The effect of amino alcohol on reducing autofluorescence.
Fig. S3. Bone CLARITY setup.
Fig. S4. Sample progression through Bone CLARITY clearing process.
Fig. S5. LSFM setup.
Fig. S6. Signal quality metrics to quantify imaging depth of Bone CLARITY.
Fig. S7. Computational pipeline.
Fig. S8. Volume comparisons in the tibia and femur.
Fig. S9. tdTomato expression in the vertebral columns.
Fig. S10. Antibody staining using Bone CLARITY.
Movie S1. Visualizing endogenous fluorescence throughout a cleared mouse femur.
Movie S2. Visualizing endogenous fluorescence throughout a cleared mouse tibia.
Movie S3. Visualizing endogenous fluorescence throughout a cleared mouse vertebral body.
Design file for the chamber holder (.stl)
Raw data values for cell counts (.xlsx)
Reference (*49*)

REFERENCES AND NOTES

1. F. Long, Building strong bones: Molecular regulation of the osteoblast lineage. *Nat. Rev. Mol. Cell Biol.* **13**, 27–38 (2012).
2. D. Goltzman, Discoveries, drugs and skeletal disorders. *Nat. Rev. Drug Discov.* **1**, 784–796 (2002).
3. P. Bianco, P. G. Robey, Skeletal stem cells. *Development* **142**, 1023–1027 (2015).
4. K. A. Klag, W. A. Horton, Advances in treatment of achondroplasia and osteoarthritis. *Hum. Mol. Genet.* **25**, R2–R8 (2016).
5. S. J. Morrison, D. T. Scadden, The bone marrow niche for haematopoietic stem cells. *Nature* **505**, 327–334 (2014).
6. T. D. Rachner, S. Khosla, L. C. Hofbauer, Osteoporosis: Now and the future. *Lancet* **377**, 1276–1287 (2011).
7. J. D. Beck, B. L. Canfield, S. M. Haddock, T. J.H. Chen, M. Kothari, T. M. Keaveny, Three-dimensional imaging of trabecular bone using the computer numerically controlled milling technique. *Bone* **21**, 281–287 (1997).
8. C. R. Slyfield, E. V. Tkachenko, D. L. Wilson, C. J. Hernandez, Three-dimensional dynamic bone histomorphometry. *J. Bone Miner. Res.* **27**, 486–495 (2012).
9. K. Chung, J. Wallace, S.-Y. Kim, S. Kalyanasundaram, A. S. Andalman, T. J. Davidson, J. J. Mirzabekov, K. A. Zalocusky, J. Mattis, A. K. Denisin, S. Pak, H. Bernstein, C. Ramakrishnan, L. Grosenick, V. Gradinaru, K. Deisseroth, Structural and molecular interrogation of intact biological systems. *Nature* **497**, 332–337 (2013).
10. H.-U. Dodt, U. Leischner, A. Schierloh, N. Jährling, C. P. Mauch, K. Deininger, J. M. Deussing, M. Eder, W. Zieglgänsberger, K. Becker, Ultramicroscopy: Three-dimensional visualization of neuronal networks in the whole mouse brain. *Nat. Methods* **4**, 331–336 (2007).
11. A. Ertürk, K. Becker, N. Jährling, C. P. Mauch, C. D. Hojer, J. G. Egen, F. Hellal, F. Bradke, M. Sheng, H.-U. Dodt, Three-dimensional imaging of solvent-cleared organs using 3DISCO. *Nat. Protoc.* **7**, 1983–1995 (2012).
12. K. Becker, N. Jährling, S. Saghafi, R. Weiler, H.-U. Dodt, Chemical clearing and dehydration of GFP expressing mouse brains. *PLOS ONE* **7**, e33916 (2012).
13. B. Yang, J. B. Treweek, R. P. Kulkarni, B. E. Deverman, C.-K. Chen, E. Lubeck, S. Shah, L. Cai, V. Gradinaru, Single-cell phenotyping within transparent intact tissue through whole-body clearing. *Cell* **158**, 945–958 (2014).
14. D. S. Richardson, J. W. Lichtman, Clarifying tissue clearing. *Cell* **162**, 246–257 (2015).
15. J. B. Treweek, K. Y. Chan, N. C. Flytzanis, B. Yang, B. E. Deverman, A. Greenbaum, A. Lignell, C. Xiao, L. Cai, M. S. Ladinsky, P. J. Bjorkman, C. C. Fowlkes, V. Gradinaru, Whole-body tissue stabilization and selective extractions via tissue-hydrogel hybrids for high-resolution intact circuit mapping and phenotyping. *Nat. Protoc.* **10**, 1860–1896 (2015).
16. E. A. Susaki, H. R. Ueda, Whole-body and whole-organ clearing and imaging techniques with single-cell resolution: Toward organism-level systems biology in mammals. *Cell Chem. Biol.* **23**, 137–157 (2016).
17. S. Calve, A. Ready, C. Huppenbauer, R. Main, C. P. Neu, Optical clearing in dense connective tissues to visualize cellular connectivity in situ. *PLOS ONE* **10**, e0116662 (2015).
18. I. M. Berke, J. P. Miola, M. A. David, M. K. Smith, C. Price, Seeing through musculoskeletal tissues: Improving in situ imaging of bone and the lacunar canalicular system through optical clearing. *PLOS ONE* **11**, e0150268 (2016).
19. C. P. Neu, T. Novak, K. F. Gilliland, P. Marshall, S. Calve, Optical clearing in collagen- and proteoglycan-rich osteochondral tissues. *Osteoarthritis Cartilage* **23**, 405–413 (2015).
20. E. A. Genina, A. N. Bashkatov, V. V. Tuchin, Optical clearing of cranial bone. *Adv. Opt. Technol.* **2008**, 267867 (2008).
21. M. Acar, K. S. Kocherlakota, M. M. Murphy, J. G. Peyer, H. Oguro, C. N. Inra, C. Jaiyeola, Z. Zhao, K. Luby-Phelps, S. J. Morrison, Deep imaging of bone marrow shows non-dividing stem cells are mainly perisinusoidal. *Nature* **526**, 126–130 (2015).
22. E. A. Susaki, K. Tainaka, D. Perrin, H. Yukinaga, A. Kuno, H. R. Ueda, Advanced CUBIC protocols for whole-brain and whole-body clearing and imaging. *Nat. Protoc.* **10**, 1709–1727 (2015).
23. K. Tainaka, S. I. Kubota, T. Q. Suyama, E. A. Susaki, D. Perrin, M. Ukai-Tadenuma, H. Ukai, H. R. Ueda, Whole-body imaging with single-cell resolution by tissue decolorization. *Cell* **159**, 911–924 (2014).
24. R. Tomer, L. Ye, B. Hsueh, K. Deisseroth, Advanced CLARITY for rapid and high-resolution imaging of intact tissues. *Nat. Protoc.* **9**, 1682–1697 (2014).
25. P. M. Carlton, Artifacts of light. *Nat. Methods* **10**, 1135 (2013).
26. E. G. Reynaud, J. Peychl, J. Huisken, P. Tomancak, Guide to light-sheet microscopy for adventurous biologists. *Nat. Methods* **12**, 30–34 (2015).
27. E. Baumgart, U. Kubitscheck, Scanned light sheet microscopy with confocal slit detection. *Opt. Express* **20**, 21805–21814 (2012).
28. T. Soeda, J. M. Deng, B. de Crombrugghe, R. R. Behringer, T. Nakamura, H. Akiyama, Sox9-expressing precursors are the cellular origin of the cruciate ligament of the knee joint and the limb tendons. *Genesis* **48**, 635–644 (2010).
29. F. Elefteriou, X. Yang, Genetic mouse models for bone studies—Strengths and limitations. *Bone* **49**, 1242–1254 (2011).
30. N. Ono, W. Ono, T. Nagasawa, H. M. Kronenberg, A subset of chondrogenic cells provides early mesenchymal progenitors in growing bones. *Nat. Cell Biol.* **16**, 1157–1167 (2014).
31. V. Howard, M. G. Reed, in *Unbiased Stereology: Three-Dimensional Measurement in Microscopy* (Garland Science/BIOS Scientific Publishers, ed. 6, 2005).
32. C. Mühlfeld, J. Hegermann, C. Wrede, M. Ochs, A review of recent developments and applications of morphometry/stereology in lung research. *Am. J. Physiol. Lung Cell. Mol. Physiol.* **309**, L526–L536 (2015).
33. H. J. G. Gundersen, E. B. Jensen, The efficiency of systematic sampling in stereology and its prediction. *J. Microsc.* **147**, 229–263 (1987).
34. H. J. G. Gundersen, E. B. V. Jensen, K. Kiêu, J. Nielsen, The efficiency of systematic sampling in stereology—Reconsidered. *J. Microsc.* **193**, 199–211 (1999).
35. R. W. Boyce, K.-A. Dorph-Petersen, L. Lyck, H. J. G. Gundersen, Design-based stereology: Introduction to basic concepts and practical approaches for estimation of cell number. *Toxicol. Pathol.* **38**, 1011–1025 (2010).

36. D. C. Sterio, The unbiased estimation of number and sizes of arbitrary particles using the disector. *J. Microsc.* **134**, 127–136 (1984).
37. H. J. G. Gundersen, Stereology of arbitrary particles. A review of unbiased number and size estimators and the presentation of some new ones, in memory of William R. Thompson. *J. Microsc.* **143**, 3–45 (1986).
38. H. J. G. Gundersen, P. Bagger, T. F. Bendtsen, S. M. Evans, L. Korbo, N. Marcussen, A. Møller, K. Nielsen, J. R. Nyengaard, B. Pakkenberg, F. B. Sørensen, A. Vesterby, M. J. West, The new stereological tools: Disector, fractionator, nucleator and point sampled intercepts and their use in pathological research and diagnosis. *APMIS* **96**, 857–881 (1988).
39. J. E. Gardi, J. R. Nyengaard, H. J. G. Gundersen, The proportionator: Unbiased stereological estimation using biased automatic image analysis and non-uniform probability proportional to size sampling. *Comput. Biol. Med.* **38**, 313–328 (2008).
40. M. Kawai, U. I. Mödder, S. Khosla, C. J. Rosen, Emerging therapeutic opportunities for skeletal restoration. *Nat. Rev. Drug Discov.* **10**, 141–156 (2011).
41. S. Taylor, M. S. Ominsky, R. Hu, E. Pacheco, Y. D. He, D. L. Brown, J. I. Aguirre, T. J. Wronski, S. Buntich, C. A. Afshari, I. Pyrah, P. Nioi, R. W. Boyce, Time-dependent cellular and transcriptional changes in the osteoblast lineage associated with sclerostin antibody treatment in ovariectomized rats. *Bone* **84**, 148–159 (2016).
42. P. Nioi, S. Taylor, R. Hu, E. Pacheco, Y. D. He, H. Hamadeh, C. Paszty, I. Pyrah, M. S. Ominsky, R. W. Boyce, Transcriptional profiling of laser capture microdissected subpopulations of the osteoblast lineage provides insight into the early response to sclerostin antibody in rats. *J. Bone Miner. Res.* **30**, 1457–1467 (2015).
43. D. W. Dempster, Osteoporosis and the burden of osteoporosis-related fractures. *Am. J. Manag. Care* **17**, S164–S169 (2011).
44. S. Shah, E. Lubeck, M. Schwarzkopf, T.-F. He, A. Greenbaum, C. H. Sohn, A. Lignell, H. M. T. Choi, V. Gradinaru, N. A. Pierce, L. Cai, Single-molecule RNA detection at depth by hybridization chain reaction and tissue hydrogel embedding and clearing. *Development* **143**, 2862–2867 (2016).
45. N. C. Shaner, P. A. Steinbach, R. Y. Tsien, A guide to choosing fluorescent proteins. *Nat. Methods* **2**, 905–909 (2005).
46. C. Pan, R. Cai, F. P. Quacquarelli, A. Ghasemigharagoz, A. Lourbopoulos, P. Matryba, N. Plesnila, M. Dichgans, F. Hellal, A. Ertürk, Shrinkage-mediated imaging of entire organs and organisms using uDISCO. *Nat. Methods* **13**, 859–867 (2016).
47. A. Aspelund, S. Antila, S. T. Proulx, T. V. Karlsen, S. Karaman, M. Detmar, H. Wiig, K. Alitalo, A dural lymphatic vascular system that drains brain interstitial fluid and macromolecules. *J. Exp. Med.* **212**, 991–999 (2015).
48. A. Louveau, I. Smirnov, T. J. Keyes, J. D. Eccles, S. J. Rouhani, J. D. Peske, N. C. Derecki, D. Castle, J. W. Mandell, K. S. Lee, T. H. Harris, J. Kipnis, Structural and functional features of central nervous system lymphatic vessels. *Nature* **523**, 337–341 (2015).
49. A. Bria, G. Iannello, TeraStitcher—A tool for fast automatic 3D-stitching of teravoxel-sized microscopy images. *BMC Bioinf.* **13**, 316 (2012).

Acknowledgments: We thank A. Lignell and L. Cai for technical help in building the LSFM and the Amgen Scientific Team (F. Asuncion, D. Hill, M. Ominsky, and E. Pacheco). A.G. is a Good Ventures Fellow of the Life Sciences Research Foundation. **Funding:** This work was supported by NIH Director's New Innovator Award (IDP20D017782) and Presidential Early Career Award for Scientists and Engineers; Heritage Medical Foundation; Curci Foundation; Amgen Chem-Bio-Engineering Award; Pew Charitable Trust; Kimmel Foundation; and Caltech–City of Hope. **Author contributions:** H.J.M. and V.G. conceived the project; A.G. and K.Y.C. performed all experiments, data acquisition, and analysis; T.D. and D.B. contributed computational tools and data analysis with input from R.B.; D.H.B. and H.M.K. contributed samples for clearing. A.G., K.Y.C., T.D., D.B., and V.G. generated the figures and wrote the manuscript with input from all authors. V.G. supervised all aspects of the work. **Competing interests:** V.G., K.Y.C., and A.G. are inventors on patent application 62/447,781 submitted by the California Institute of Technology that covers methods and devices for soft and osseous tissue clearing and fluorescence imaging. H.J.M. and R.B. are employees and shareholders of Amgen. All other authors declare that they have no competing interests. **Data and materials availability:** The r13c7 antibody can be provided by and at Amgen's sole discretion, with pending scientific review and a completed material transfer agreement with Amgen. Requests for antibody from an academic or nonprofit institution should be submitted to www.ext.amgen.com/partners/academic-collaborations/new-requests/. Requests for antibody from a for-profit entity should be submitted to BDopportunities@amgen.com.

Submitted 27 July 2016
Accepted 23 March 2017
Published 26 April 2017
10.1126/scitranslmed.aah6518

Citation: A. Greenbaum, K. Y. Chan, T. Dobreva, D. Brown, D. H. Balani, R. Boyce, H. M. Kronenberg, H. J. McBride, V. Gradinaru, Bone CLARITY: Clearing, imaging, and computational analysis of osteoprogenitors within intact bone marrow. *Sci. Transl. Med.* **9**, eaah6518 (2017).

Science Translational Medicine

Bone CLARITY: Clearing, imaging, and computational analysis of osteoprogenitors within intact bone marrow

Alon Greenbaum, Ken Y. Chan, Tatyana Dobreva, David Brown, Deepak H. Balani, Rogely Boyce, Henry M. Kronenberg, Helen J. McBride and Viviana Gradinaru

Sci Transl Med **9**, eaah6518.
DOI: 10.1126/scitranslmed.aah6518

Peeking in on osteoprogenitors

The eyes may be the windows to the soul, but a window into the bone—specifically bone marrow—would be useful for studying bone development and disease. Greenbaum *et al*. developed a method of whole-bone optical clearing, using a series of reagents under continuous flow to delipidate and decalcify bone tissue. This process renders the entire bone transparent but does not affect endogenous fluorescence, making this compatible with reporter mice. Using light sheet fluorescence microscopy, the authors counted and mapped the number of fluorescently labeled osteoprogenitors within cleared mouse tibia, vertebral column, and femur bones treated with sclerostin antibody. With reduced variability compared to standard section analysis, this Bone CLARITY and computational analysis will be a useful tool for bone research.